A *DQ*-Frame Asymmetrical Virtual Impedance Control for Enhancing Transient Stability of Grid-Forming Inverters

Zheming Jin, *Member, IEEE*, and Xiongfei Wang, *Senior Member, IEEE*

***Abstract*—This article proposes a *dq*-frame asymmetrical virtual impedance control scheme for preventing grid-forming (GFM) inverters from the loss of synchronization with the grid under large disturbances. The approach exploits the two degrees of freedom in the *dq*-frame virtual impedance synthesis of GFM inverters, and introduces a virtual transient impedance (VTI) scheme to improve the power transmission capability and, thus, restoring equilibrium points of GFM inverters during the large disturbances. The transient stability of GFM inverters with the different kinds of virtual impedance setting is analyzed to formulate the design guideline of VTI method. Simulations and experimental tests are presented to validate the effectiveness of the approach.**

***Index Terms*—Grid-forming (GFM) inverters, synchronous reference frame, transient stability, virtual impedance.**

I. Introduction

THE INVERTER-BASED renewable energy sources are gradually replacing fossil-fueled power stations that use synchronous generators [1]. To accommodate the increasing penetration of inverter-based sources, grid-forming (GFM) inverters that are controlled as voltage sources are demanded by power system operators [2]–[4]. Recent studies have found that GFM inverters have better stability robustness than grid-following inverters in weak grids [5]–[7], yet they may lose synchronism with the grid under large disturbances, e.g., grid faults [8]–[11]. Such loss of synchronization (LOS) phenomena are also known as transient stability issues [12].

The research work on the transient stability analysis of GFM inverters is increasingly reported in recent years. Similar to synchronous generators, the existence of equilibrium points (EPs) is a necessary condition for keeping the synchronization of GFM inverters under large disturbances [13]. The transient stability issues are thus classified into the following two types [13], 1) the Type-I transient stability with EPs after the disturbance, and 2) the Type-II transient stability without EP. Yet, unlike synchronous generators, the EPs of GFM inverters are dependent on their used control schemes, since the sensitive parameters, such as droop coefficient, inertial constant, power reference, and output impedance feature, are all programmable in GFM inverters.

There has been some research work reported to enhance the transient stability of GFM inverters. It has been shown that the Type-I transient stability problem can be mitigated by adaptively tuning the parameters of active power controller [14]–[16], or by using a mode-adaptive control to change the sign of control loop gain from positive to negative when the EP of the system enters the unstable region [17]. However, for the Type-II transient stability issue, there still lack an effective approach to restoring the EPs of GFM inverters.

Further, to preserve the voltage-source characteristic of GFM inverters during grid faults, the virtual impedance (VI) control is commonly used to limit the overcurrent of GFM inverters. In [10] and [18], the impact of VI on transient stability of GFM inverters is discussed. The results indicate that a large VI can help limit the fault current [18], [19], yet it may jeopardize the transient stability performance due to the reduced power transmission margin (PTM) [10].

To avoid the adverse effect of VI on the transient stability, this article proposes an alternative way to utilize the VI control. The general idea is to synthesize the VI in the *dq*-frame, and then apply different VI setting at the *d*- and *q*-axis, such that an additional degree of freedom in the VI control can be introduced. With the asymmetrical *dq*-frame VI, the power–angle relationship, which is critical to the transient stability of GFM inverters, can be reshaped, and the different impact of *d*- and *q*-axis VI on the PTM can be utilized. Further, a virtual transient impedance (VTI) control is developed to restore the EPs during severe grid faults, such that the Type-II transient instability can be prevented. Time-domain simulations and experimental tests are performed to verify the effectiveness of proposed approach.

Manuscript received May 28, 2021; revised September 12, 2021; accepted October 16, 2021. Date of publication November 2, 2021; date of current version December 31, 2021. Recommended for publication by Associate Editor M. Hartmann. *(Corresponding author: Xiongfei Wang.)*

Zheming Jin is with the School of Electrical Engineering, Beijing Jiaotong University, Beijing, China (e-mail: zhmjin@bjtu.edu.cn).

Xiongfei Wang is with the Department of Energy Technology, Aalborg University, 9220 Aalborg East, Denmark (e-mail: xwa@energy.aau.dk).

Color versions of one or more figures in this article are available at https://doi.org/10.1109/TPEL.2021.3124286.

Digital Object Identifier 10.1109/TPEL.2021.3124286

II. Transient Stability Problem of GFM Inverters

A. System Description of Benchmark Study Case

Fig. 1 shows a general system diagram of a grid-connected GFM inverter, which is integrated into the power grid through a transformer and two paralleled transmission lines. $L_{\rm leak}$ and Z_{T1}–Z_{T3} represent the leakage inductance of transformer and

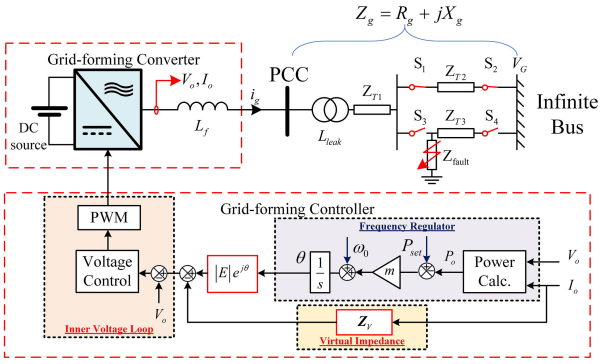

Fig. 1. System diagram of the benchmark study case of this article: a generalized grid-connected GFM inverter with transmission margin change due to fault.

the transmission line impedances, respectively. V_o and I_o denote the output voltage and output current vectors of the GFM inverter, respectively. Since the main concern of this work is focused on the control of GFM inverter, the passive components beyond point of common coupling are simplified as equivalent impedance ($Z_g = R_g + jX_g$). In addition, the optional grid-side inductor L_f is also considered as a part of Z_g. A symmetrical three-phase-to-ground fault is considered as the grid disturbance, which results in an increase of the equivalent impedance Z_g and reduced PTM [8], [13].

An inner voltage control loop is needed to regulate the output voltage V_o of the GFM inverter, whose voltage reference is determined by the outer power control loop and the virtual impedance loop. It is noteworthy that the inner voltage control loop is usually designed with a much faster dynamic when compared with the outer power control loop [20], [21]. As the transient stability is mainly determined by the dynamic of outer power control loop, the inner voltage loop is assumed to have ideal reference-tracking performance in this study.

In this work, active power–frequency droop is considered as the frequency regulation method, since the optional inertia emulation has no influence on the power–angle relationship and PTM [8], [14], [15]. Nevertheless, an inductive VI is also adopted in the control system of GFM inverter for the following three reasons.

1) The GFM control scheme will naturally require a minimum line impedance; otherwise, its stability will be poor [9]. Meanwhile, this VI will increase the equivalent *X/R* ratio of the inverter–grid system, which helps to ensure decoupled active power–frequency regulation.
2) VI has significant impact and can be utilized for reactive power sharing among paralleled GFM inverters [22].
3) VI has natural capability to limit the transient current, which is also a commonly used current limitation method during large grid disturbance [18], [19].

In this sense, a virtual inductor is considered for normal-state operation of the studied GFM inverter.

B. Transient Stability Problem of the GFM Inverter

In Fig. 2, the equivalent circuit of the GFM inverter connected to power grid is presented, in which the GFM inverter

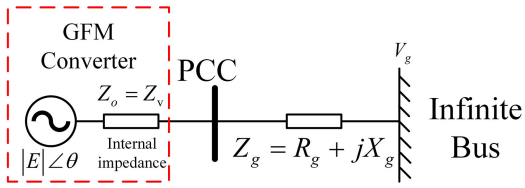

Fig. 2. Equivalent circuit of benchmark study case.

is represented by a controlled-voltage source behind an internal impedance. The internal-voltage source is regulated by the active power control loop with a fixed voltage magnitude, whereas the internal impedance is determined by VI loop.

By defining the equivalent impedance Z_Σ of the transmission circuit and phase angle difference between the internal-voltage source and the infinite bus δ, which are given by

$$\begin{cases} Z_\Sigma = Z_g + Z_V = R_\Sigma + jX_\Sigma \\ \delta = \theta - \theta_g \end{cases}. \tag{1}$$

By considering the normal-state virtual inductor, the *X/R* ratio of the equivalent circuit will be high enough to neglect the stray resistor. In this case, the power–angle relationship of the grid-connected GFM inverter can be expressed as

$$P_o(\delta) = \frac{|E||V_g|}{X_\Sigma}\sin\delta = P_M \sin\delta \tag{2}$$

where P_M denotes the PTM of the GFM inverter [13].

The P_o–δ curve is shown in Fig. 3. It can be easily found that the P_o–δ relationship is a nonmonotonic function in the range of $0 \leq \delta \leq \pi$. P_o will first increase to its maximum value, i.e., the P_M, and then decrease to zero. Thus, the P_o–δ relationship is divided into stable and unstable regions, where the presence of unstable region is the root cause of the transient instability phenomenon of the GFM inverter and conventional SG [13].

Based on different severity of the fault, the transient stability problems can be further divided into two types, depending on whether the system has EPs after a grid disturbance; both are illustrated, as shown in Fig. 3.

1) *Type-I transient stability problem (with EPs):* The P_o–δ relationship of the Type-I transient stability problem is shown in Fig. 3(a). In this case, EPs exist after the large disturbance, in which a stable EP (SEP) and an unstable EP (UEP) exist in the two regions, respectively. When large grid disturbance occurs, the operating point will move from *a* to *b* immediately due to fault. Driven by the power unbalance (i.e., $P_o < P_{\text{ref}}$) after the large grid disturbance, the output frequency of GFM inverter will further increase and, thus, the operating point will move from *b* to the SEP *c*. At this point, the operating point will keep moving toward the UEP *e*, due to the presence of delay or inertia contribution of GFM controller [10]; however, the movement is deaccelerating due to reverse power unbalance (i.e., $P_o > P_{\text{ref}}$). In this case, the system will recover and stabilize if the operating point does not crossover the UEP *e*; otherwise, the frequency will increase again and leads to LOS. The equal area criterion suggests that with larger deaccelerating zone, the SG or GFM inverter will have more chance to be stable [13].

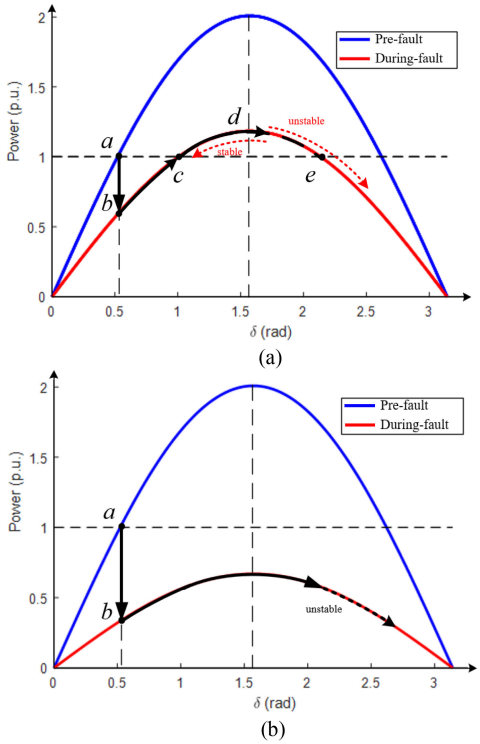

Fig. 3. Movement of operating point under large grid disturbance. (a) Type-I transient stability problem. (b) Type-II transient stability problem.

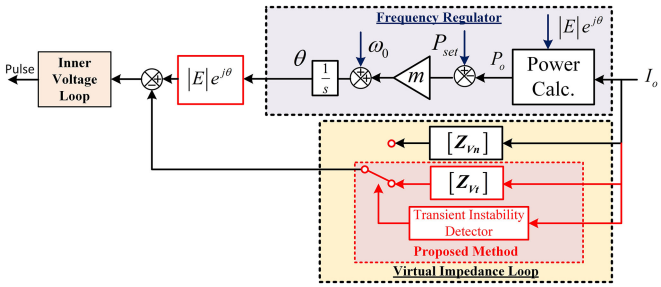

Fig. 4. Block diagram of the GFM control with the proposed VTI scheme.

2) Type-II transient stability problem (without EP): The P_o–δ relationship of the Type–II transient stability problem is shown in Fig. 3(b). In this scenario, the severity of grid fault is even worse than that of the Type I. The during-fault P_o–δ curve has no EPs, so that the frequency of GFM inverter will be continuously increasing and leads to LOS directly.

III. Proposed Asymmetrical VTI Control Method

Fig. 4 presents the overall control diagram of the proposed method. The proposal can be considered as a mode-switching VI loop. In normal operation, the normal-state VI, i.e., $\boldsymbol{Z}_{Vn}$, will be performed to regulate the GFM inverter, as shown in Fig. 1. During the large grid disturbance, the VI control loop will be switched to the proposed VTI control method using dedicated *dq*-frame asymmetrical VTI, i.e., $\boldsymbol{Z}_{Vt}$, to perform the fault-ride-through. To deploy the proposed control correctly, a transient instability detector is also proposed to detect the LOS phenomenon and, thus, control the timing of mode switching.

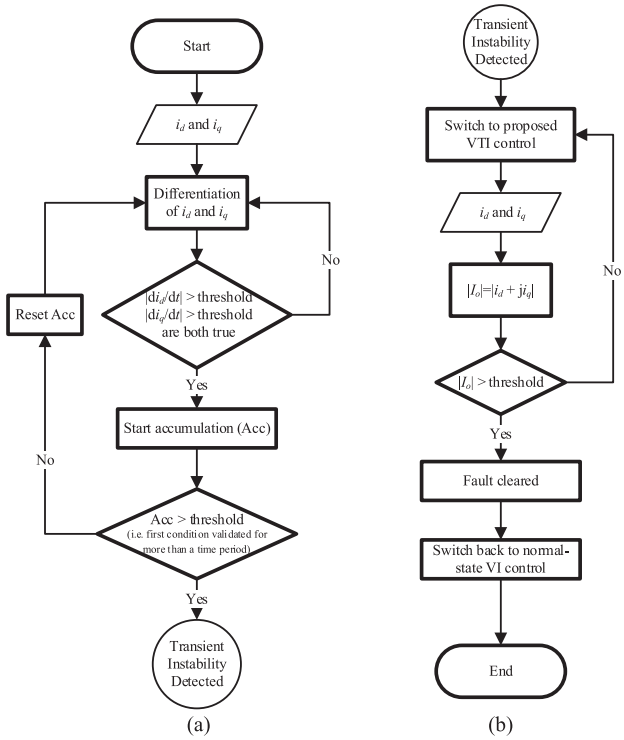

Fig. 5. Overall flowchart of proposed method. (a) Transient instability detection algorithm. (b) Reaction based on the proposed control method.

The overall flowchart of the proposed control method is shown in Fig. 5, including both the transient instability detection and the fault reaction by utilizing the proposed VTI method.

In addition, in this study, the power calculation is based on internal-voltage reference. This slight change has been adopted in recent research [23] and will have no influence on the normal operation if the virtual inductor is used (i.e., benchmark study case). However, by doing so, the behavior of the frequency regulator can be based on the interaction between the two voltage sources (i.e., E and V_g are shown in Fig. 2) correctly.

The main concern of the proposal is the Type-II severe grid disturbance without EPs, in which the existence of EP shall be restored to meet the necessary prerequisite of transient stability at first place. For this reason, the proposed method is focused on increasing the during-fault PTM by introducing especially designed *dq*-frame asymmetrical VTI, and, thus, stabilizing the GFM inverter by reobtaining EPs. In the following parts of this section, the principle of the transient instability detector used in the proposal and impact of the proposed *dq*-frame asymmetrical VTI on the PTM of the system are both presented in detail.

A. Principle of Transient Instability Detection

By considering the feeder line dynamic of the equivalent circuit shown in Fig. 2, the output current of the GFM inverter under its own *dq*-reference frame can be expressed by

$$\begin{cases} L_g \frac{\mathrm{d}i_d}{\mathrm{d}t} + r_g i_d = (|E| - |V_g|\cos\delta) + (\omega L_g + X_v) i_q \\ L_g \frac{\mathrm{d}i_q}{\mathrm{d}t} + r_g i_q = (0 + |V_g|\sin\delta) - (\omega L_g + X_v) i_d \end{cases} \quad (3)$$

where L_g denotes the physical inductance of the feeder line, ω denotes the frequency of GFM inverter, and r_g stands for the inevitable stray resistance, which is small and neglectable.

The right-hand side is also known as the quasi-steady-state phasor relationship, whereas the left-hand side suggests a natural delay due to feeder line dynamic. In addition to this natural delay, there will also be a low-pass filter and/or inertia and damping emulation control in the frequency regulation loop of the GFM inverter, which also forms a first-order delay [10].

With the first-order delay characteristic, the frequency regulation function can be presented by

$$\begin{cases} \omega = \omega_0 + mP_{set} - mP_{cal} \\ P_{cal} = \frac{1}{\tau s+1} P_o(\delta) \end{cases} \tag{4}$$

where $P_{\rm cal}$ denotes the calculated output power for frequency regulation and $P_o(\delta)$ denotes the active power derived by phasor derivation, a simplified form of which has been shown as (2).

The frequency regulation function (4) can be rewritten into a differential equation

$$H\dot{\omega} = P_{set} - P_o(\delta) - D(\omega - \omega_n) \tag{5}$$

where $H = \tau$/m denotes the inertial constant, $D = 1$/m denotes the damping factor, and ω_n is the nominal frequency of the inverter. In this study, we consider $\omega_n = \omega_g$ and both are constant (100 π rad/s, i.e., 50 Hz). In which the power angle and its first- and second-order differentiation can be further expressed by

$$\begin{cases} \delta = \theta - \theta_g = \int (\omega - \omega_g) \mathrm{d}t + \delta_0 \\ \dot{\delta} = \omega - \omega_g \\ \ddot{\delta} = \dot{\omega} = \frac{1}{H} \left[P_{set} - P_o(\delta) - D(\omega - \omega_n) \right] \end{cases} \tag{6}$$

where δ_0 denotes the initial phase between two voltage vectors.

It can be seen from (3) that the output current and its first-order differentiation are both connected with the power angle dynamic. By substituting (6) into (3), the relationship between current and power angle dynamic can be detailed as

$$\begin{cases} L_g \frac{\mathrm{d}i_d}{\mathrm{d}t} + r_g i_d = (|E| - |V_g| \cos\delta) + \underbrace{(\omega_{\rm g} L_g + X_v)}_{X_\Sigma} i_q \\ \qquad\qquad + \frac{\mathrm{d}\delta}{\mathrm{d}t} L_g i_q \\ L_g \frac{\mathrm{d}i_q}{\mathrm{d}t} + r_g i_q = (0 + |V_g| \sin\delta) - \underbrace{(\omega_{\rm g} L_g + X_v)}_{X_\Sigma} i_d - \frac{\mathrm{d}\delta}{\mathrm{d}t} L_g i_d \end{cases} \tag{7}$$

As the movement of operating point is typically with slow dynamic, it is reasonable to neglect the first two terms of the right-hand side. In this sense, the current–angle relationship can be approximated as

$$\begin{cases} \frac{\mathrm{d}i_d}{\mathrm{d}t} \propto \frac{\mathrm{d}\delta}{\mathrm{d}t} i_q \\ \frac{\mathrm{d}i_q}{\mathrm{d}t} \propto -\frac{\mathrm{d}\delta}{\mathrm{d}t} i_d \end{cases} . \tag{8}$$

By (8), a natural indicator of the equivalent movement of δ can be obtained by calculating the first-order differentiation of both i_d and i_q. It is noteworthy that for normal load swing, the movement of δ will be stopped soon after the system reaches its new SEP, whereas the movement will maintain continuously if the transient instability occurs (see Fig. 9 and Section IV-A). This feature forms the fundamental of the detection algorithm of transient instability (i.e., LOS phenomenon), which is detailed in the following part of this section.

B. Implementation of the Transient Instability Detector

As discussed in previous sections, the detection of transient stability is essential to detect the LOS phenomenon, which can be indicated by continuous change in both i_d and i_q. Based on this principle, a detection algorithm of transient instability phenomenon can be derived, the flowchart of which has been shown in Fig. 5(a).

To properly detect the continuous movement of the operating point as the feature of LOS, the proposed transient instability detector checks the magnitude of the first-order differentiation of both i_d and i_q. If the operating point is changed, the rate of change of current (i.e., $|di_d/dt|$ and $|di_q/dt|$) will both have a pulsed change. Yet, if stable, the movement of operating point will follow the first-order characteristic and they will decay in respect of the time constant of the system [24]. In addition, the operating point movement on the P_o–δ relationship curve in the stable region is mainly driven by the change of P_o and i_d, the change of i_q will be naturally smaller and decay in a faster dynamic. For this reason, the magnitude threshold to detect can be set mainly according to i_q. As for the time threshold [i.e., ACC in Fig. 5(a)], the system dynamic will follow a first-order characteristic, and the time constant of this dynamic can be utilized to design the time threshold.

It is noteworthy that the influence of line impedance is considerable for setting the threshold due to its impact on the rate of the change of the output current and the time constant of the system dynamic. However, these parameters can be tested when GFM inverters are installed and they will not change if the system is not changed. Hence, the proposed transient stability detector is possible to be implemented without knowledge on exact value of the transmission line impedance.

As for the fault clearance, in case that the proposed VTI control has successfully prevented LOS, the system will operate at mostly full power with large δ over normal operation. In this case, a short-term overcurrent will occur when fault is cleared due to the sudden decrease of the line impedance. It is worthy to notice that during the transmission line fault, which is the focused-study case of this work, the output current of the converter will be reduced during the fault due to increased line impedance. Hence, the overcurrent will only occur if the fault is cleared, which makes it a natural indicator for fault clearance.

C. Impact of Different VTI Design on Transmission Margin

As suggested in [10], the PTM of the GFM inverter is influenced by both transmission line impedance and the VI. In Fig. 6(a), the P_o–δ curve of a grid-connected GFM inverter with commonly used inductive and resistive VI are both presented. It can be found that virtual inductor will reduce the PTM, whereas the virtual resistor will increase the PTM. However, a large resistor will be needed in this scenario, it has been widely reported that the reduced *X/R* ratio of the equivalent transmission line will lead to a stronger coupling effect between the active

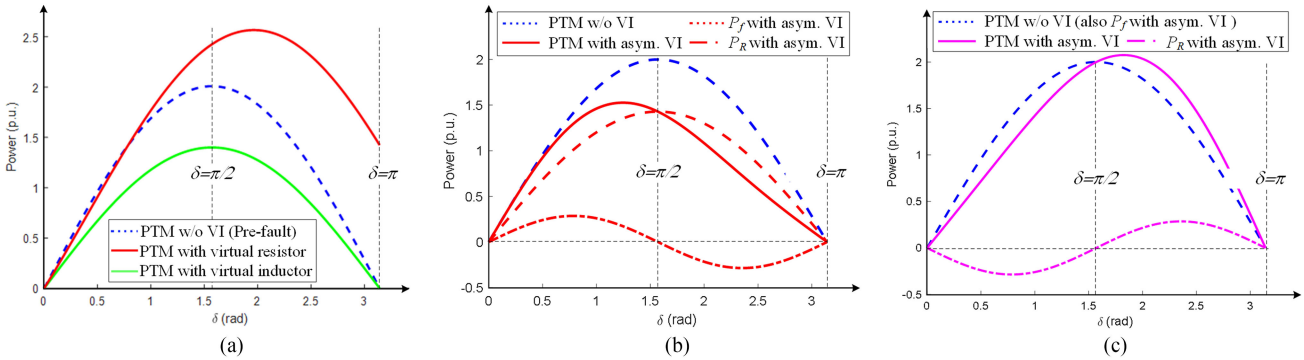

Fig. 6. Transmission margin with different virtual impedance design. (a) Symmetrical virtual resistor $R_v = 0.2$ p.u., and virtual inductor $X_v = 0.2$ p.u. (b) *dq*-frame asymmetrical inductor with $X_d = 0.7$ p.u. and $X_q = 0.5$ p.u. (c) *dq*-frame asymmetrical inductor with $X_d = 0.5$ p.u. and $X_q = 0.7$ p.u.

TABLE I
COMPARISON BETWEEN DERIVED IMPEDANCE DESIGNS

Method	Virtual resistor (VR)	Symmetrical virtual impedance (*sym.* VC)	Asymmetrical virtual impedance #1 (*asym.* VI #1)	Asymmetrical virtual impedance #2 (*asym.* VI #2)	Asymmetrical virtual impedance #3 (*asym.* VI #3)
d-axis impedance	Resistance (positive)	Reactance (negative)	Reactance (negative)	zero	Reactance (negative)
q-axis impedance	Resistance (positive)	Reactance (negative)	zero	Reactance (positive)	Reactance (positive)
d-axis terminal voltage (under positive i_d and i_q)	Reduced(<*E*)	Increased (>*E*)	No change (=*E*)	reduced(<*E*)	reduced(<*E*)
q-axis terminal voltage (under positive i_d and i_q)	Increased (>0)	Increased (>0)	Increased (>0)	No change (=0)	Increased (>0)
Voltage magnitude	reduced	significantly increased	increased	reduced	reduced
Transmission margin	increased	increased	increased	slightly increased	significantly increased
Decoupled *P-f* regulation	No [24]	Yes	Yes	Yes	Yes

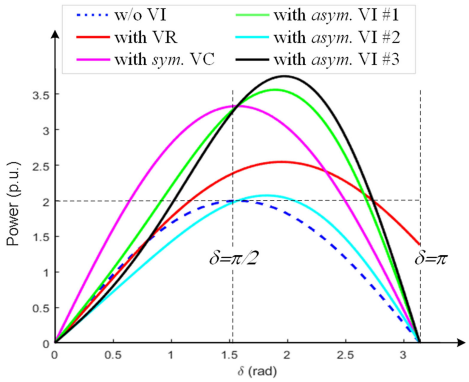

Fig. 7. PTM with derived impedance designs. (Line impedance set to be 0.5 p.u., VI set to be 0.2 p.u. per axis.)

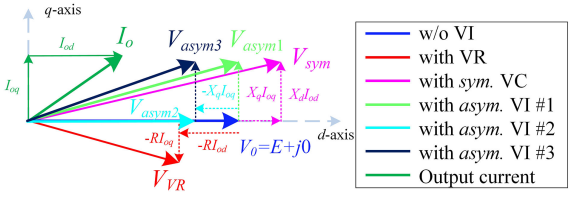

Fig. 8. Voltage vector of GFM inverter before and after adopting different impedance designs.

power and reactive power regulation; thus, the synchronization stability and the frequency regulation will both be affected [25].

Besides these commonly used VI design, the power system and electric machine study have both indicated that the internal impedance of an SG can be complicated and asymmetrical. A famous example is the salient-pole synchronous machine, the internal impedance of which is *dq*-frame asymmetrical due to its unique structure. The asymmetricity results in the reluctance torque, which is additional second-order P_o–δ relationship. The P_o–δ relationship of such a generator can be expressed by the following [26]:

$$P_o = (E + i_q X_q) i_d + (0 - i_d X_d) i_q = E i_d + i_d i_q (X_q - X_d)$$
$$= \underbrace{\frac{|E|\,|V_g|}{X_d}\sin\delta}_{P_f} + \underbrace{\frac{|V_g|\sin\delta}{X_d}\frac{|E| - |V_g|\cos\delta}{X_q}(X_q - X_d)}_{P_R} \quad (9)$$

where the X_d and X_q stands for the *d*- and *q*-axis internal reactance of the SG, respectively. The first term represents the fundamental P_o–δ relationship (marked as P_f), the rest of the term is introduced by the reluctance P_o–δ relationship (marked as P_R).

It can be found that the commonly used P_o–δ relationship (2) is a simplification of (9) under assumption $X_d = X_q = X$. In Fig. 6(b) and (c), the P_o–δ curve under two kinds of asymmetricity, i.e., $X_d > X_q$, and $X_d < X_q$, are shown. It can be seen from the results that the presence of P_R will increase the PTM, i.e., the peak value of the P_o–δ curve, but the peak value will no longer appear at the point $\delta = \pi/2$. Meanwhile, the analytical results shown in both Fig. 6(b) and (c) indicated that, no matter implemented by symmetrical or asymmetrical VI, the

presence of the positive *d*-axis reactance will reduce the PTM as it is affecting P_f significantly. Thus, it suggests that the *d*-axis negative reactance (i.e., capacitive reactance) will be also helpful to improve the PTM. In addition to that, with proper design, the first monotonic region of the P_o–δ curve can be enlarged [see Fig. 6(c)], which provides an additional stability buffer region for the power angle movement under grid disturbance.

Based on the theoretical analysis, five different impedance designs can be derived to enhance the PTM, which are listed as follows.

1) *Virtual resistor* (VR): positive virtual resistor.
2) *Symmetrical virtual capacitor* (*sym.* VC): symmetrical virtual capacitor (i.e., negative virtual reactance).
3) *Asymmetrical VI #1* (*asym.* VI #1): negative virtual reactance on the *d*-axis only;
4) *Asymmetrical VI #2* (*asym.* VI #2): positive virtual reactance on the *q*-axis only;
5) *Asymmetrical VI #3* (*asym.* VI #3): combination of *asym.* VI #2 and *asym.* VI #3.

A comparison of these derived impedance designs regarding their influence on different control variables is presented in Table I, and a quantitative comparison of their PTM are given in Fig. 7, in which the physical transmission impedance is set to be 0.5 p.u., and the value of VI are set to be 0.2 p.u. for each of these derived impedance designs.

It is noteworthy that the value of impedance discussed in this article is relatively large when compared to normal-purpose virtual impedance. Hence, it is necessary to take the voltage magnitude after adopting VI into consideration, as the GFM inverter has its physical limitation on its maximum output voltage. In Fig. 8, the voltage–vector relationship of GFM inverter's output voltage is illustrated. It can be seen from the analytical results shown in Figs. 7 and 8 that the impedance design *asym* VI #3 will provide the greatest improvement on PTM with reduced output voltage magnitude. For this reason, the impedance design *asym* VI #3 is selected as the VTI control method of this article.

It is also important to notice that the increase of PTM will be affected by both the line impedance and the VTI design. Hence, it is impossible to give an optimal design regarding the *d*- and *q*-axis VTI for all cases. However, a feasible range of VTI can be given according to the line impedance feature of Type-II transient instability issue. As mentioned in Section II, the line impedance when LOS occurs will be always larger than 1.0 p.u., which gives an upper limitation of the VTI.

In this work, the VTI is set to have equal absolute value of virtual reactance in *d*- and *q*-axis following the principle of *asym* VI #3. The reactance is in the range of 0.5–0.7 p.u. to provide significant increase on PTM without losing necessary margin and conservativity for real-world implementation.

IV. Simulation Validation

In this section, time-domain simulations are performed to demonstrate and to verify the effectiveness of the proposed asymmetrical VTI control method. The benchmark study case shown in Fig. 1 is simulated, in which the major parameters are given in Table II. It is noteworthy that inner-voltage control loop and current limitation are both used in the simulation, and the results, as will be shown in the following parts, justify the prior-assumption made in Sections II and III when presenting the transient stability issue of GFM inverters and deriving the proposed VTI control method.

TABLE II
Parameters for Simulation Study Case

Parameter	Symbol	Value
Grid voltage	V_g	220V (1.0 p.u.)
Nominal voltage magnitude	E_n	220V (1.0 p.u.)
Nominal system frequency	f_n	50Hz
Rated capacity of GFM converter	S_0	100kVA (1.0 p.u.)
P-f droop coefficient	m	0.04 p.u.
Virtual impedance in normal operation	X_{Vn}	1mH (0.22 p.u.)
Converter-side inductor of *LC* filter	L_s	1mH
Filter capacitance of *LC* filter	C_f	10μF
Switching frequency	f_{sw}	20kHz
Proportional gain of current loop	K_{pc}	3
Proportional gain of voltage loop	K_{pv}	200
Resonance gain of voltage loop	K_{pv}	20000
Pre-fault transmission line impedance	L_{g_pre}	2.3 mH (0.49 p.u.)
In-fault transmission line impedance	L_{g_fault}	6.9 mH (1.49 p.u.)
Post-fault transmission line impedance	L_{g_post}	2.3 mH (0.49 p.u.)
Detector magnitude threshold	I_T	1.5
Detector time threshold	t_D	0.05s
Current limitation	I_{max}	300A
d-axis VTI	X_{Td}	-1Ω (0.67 p.u.)
q-axis VTI	X_{Tq}	1Ω (0.67 p.u.)

A. Verification of the Proposed Transient Instability Detection

In this part, the proposed transient instability detector is first verified. In Fig. 9, the active power, *d*- and *q*-axis current (with its first-order differentiation), and frequency dynamic of the GFM inverter before and during the fault are presented. At $t = 0$ s, the GFM inverter starts working with a zero-power setpoint. At $t = 0.2$ s, a 0%–100% load step is performed by power setpoint change; at $t = 0.4$ s, a 100%–0% load step is performed by power setpoint change; at $t = 1.0$ s and $t = 1.5$ s, two 50% load steps are performed. At $t = 2.0$ s, the transmission line fault occurs and the line impedance increased from 0.49 to 1.49 p.u.; thus, the short-circuit ratio (SCR) of the system falls from 2.02 down to 0.68. In this case, the GFM inverter suffers from the LOS problem due to nonexistence of EP. Hence, both active power and output current are continuously resonating due to the change of angle δ with a low-frequency behavior. At $t = 4.5$ s, the transmission line fault is cleared, whereas an overcurrent (together with overpower) happens to the system.

It can be seen from the simulation results that the first-order differentiation of i_d and i_q show significantly different feature during the load steps (after $t = 0.2$, 0.4, 1.0, or 1.5 s) and the transient instability (after $t = 2.0$ s). During the load steps, the di_d/dt has a very large magnitude and attenuate in a time scale equal to the response time of power control, whereas the di_q/dt has small magnitude and attenuate fast. However, after LOS due to grid disturbance, both di_d/dt and di_q/dt will be continuously resonating with a similar scale of magnitude, this feature is utilized to distinguish the transient instability out of normal load

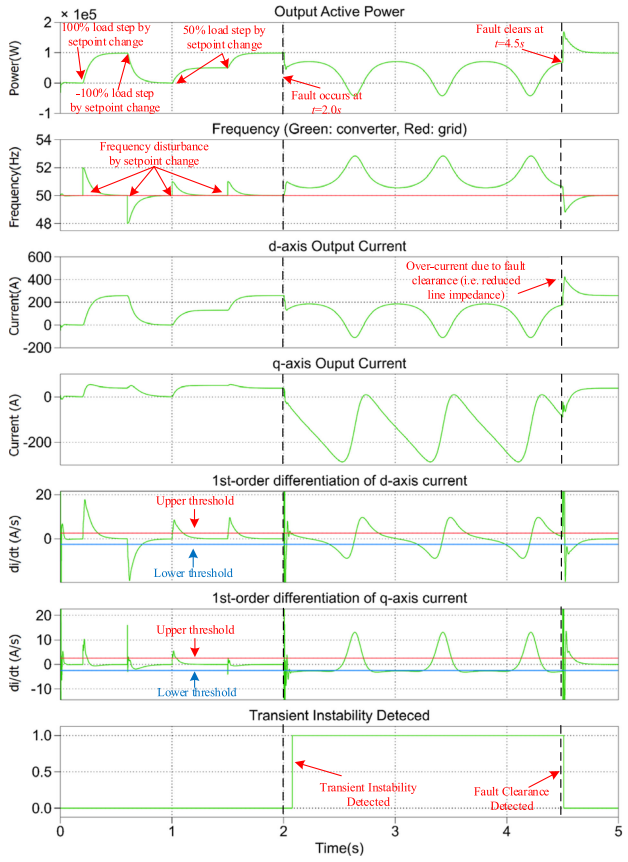

Fig. 9. Power, current, and frequency dynamic before and after simulated grid disturbance.

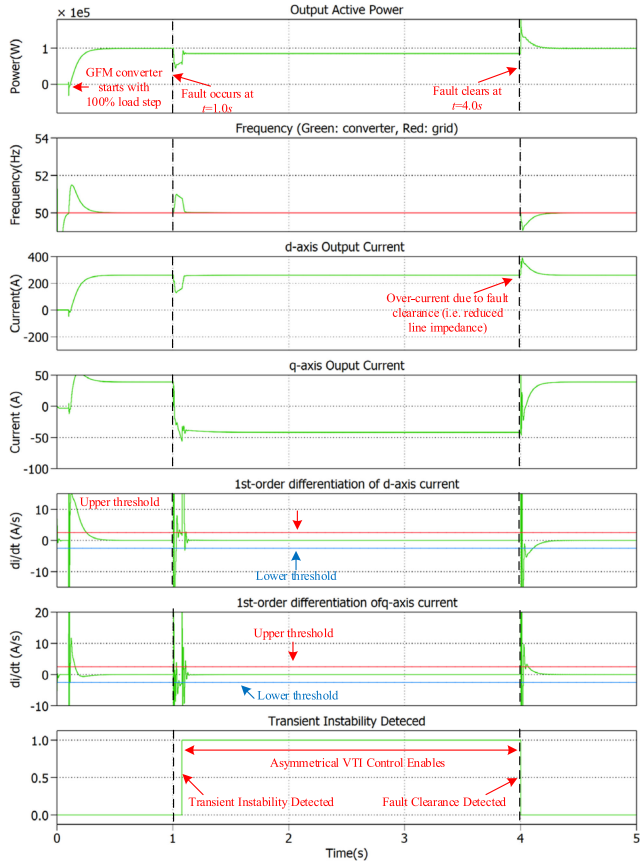

Fig. 10. Power, current, and frequency dynamic before and after simulated grid disturbance.

swing. It can be found that the proposed detection method can easily detect the LOS phenomenon during transient instability; moreover, it can distinguish the LOS from all kinds of large and small load swing.

By adopting the proposed transient instability detection method (see Fig. 5), the LOS is effectively detected at its early stage. In this simulation scenario, the total time delay of the proposed detection method is 0.08 s, which is much smaller when compared with the resonance cycle of the output power due to the LOS phenomenon.

B. Validation of the Proposed Asymmetrical VTI Control Method

In this part, the proposed asymmetrical VTI control method is validated for transient stability enhancement. In Fig. 10, the active power, output current, and frequency dynamic of a GFM inverter with the proposed asymmetrical VTI control method are presented. In this simulation scenario, the GFM inverter employs both the normal-state VI control and the proposed asymmetrical VTI for transient stability enhancement. At $t = 0.1$ s, the GFM inverter starts working with a 0%–100% load step. At $t = 1.0$ s, the transmission line fault occurs and the line impedance increased from 0.49 to 1.49 p.u.; thus, the SCR of the system falls from 2.02 down to 0.68 and the equivalent SCR (eSCR), which considers both the line impedance and the normal-state VI of the GFM inverter, falls from 1.41 down to 0.47. Hence, the GFM inverter starts to lose synchronism with the grid. However, the proposed transient instability detector made an effective detection of the transient instability with a total time delay of 0.077 s.

After detecting the transient instability phenomenon, the proposed asymmetrical VTI is activated and replaced the normal-state VI. By comparing results in Figs. 9 and 10, it can be easily found that the PTM of the GFM inverter is increased by adopting the proposed method. With this increased PTM, the synchronism with the main grid is restored; thus, both output power and output current are regulated as a constant value. The simulation results matched with analytical results in Section III, and this validates the effectiveness of the proposed method.

V. Experimental Results

In this section, experimental results are presented to validate the effectiveness of the proposed asymmetrical VTI control method for transient stability enhancement of the GFM inverter. The configuration of the experimental setup is presented in Fig. 11. The experiment is carried out with a three-phase grid-connected GFM inverter with downscaled voltage and power rating, the major parameter of which are listed in Table III. In addition, the power angle is calculated based on the phase of V_g through a PLL and the internal angle reference θ by

$$\delta = \theta - \theta_g. \tag{10}$$

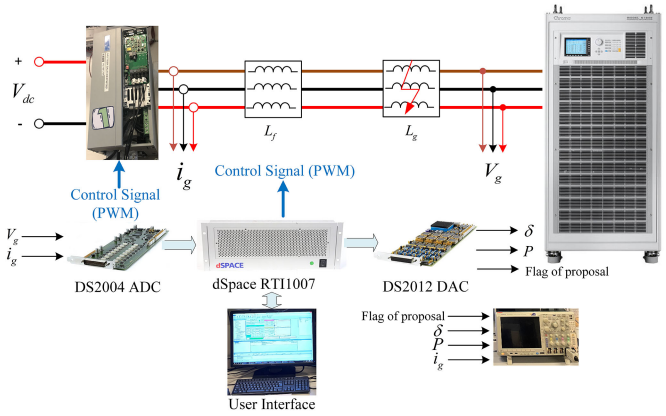

Fig. 11. Configuration of the experimental setup.

TABLE III
PARAMETERS FOR EXPERIMENT

Parameter	Symbol	Value
Grid voltage	V_g	50V (1.0 p.u.)
Nominal voltage magnitude	E_n	50V (1.0 p.u.)
Nominal system frequency	f_n	50Hz
Rated capacity of GFM inverter	S_0	1kVA (1.0 p.u.)
P-f droop coefficient	m	0.01 p.u. (test 1) 0.02 p.u. (test 2)
Grid-side filter inductor	L_f	3mH (0.20 p.u.)
Virtual impedance in normal operation	L_{Vn}	3mH (0.20 p.u.)
Pre-fault grid impedance	L_{g_pre}	11.2 mH (0.75 p.u.)
Post-fault grid impedance	L_{g_post}	14.2 mH (0.96 p.u.)
Switching frequency	f_{sw}	10kHz
Detector magnitude threshold	I_T	0.05
Detector time threshold	t_D	0.2s (in Fig.15) 1.5s (in Fig.16)
d-axis VTI	X_{Td}	-2.4Ω (0.51 p.u.)
q-axis VTI	X_{Tq}	2.4Ω (0.51 p.u.)

It is noteworthy that the power angle δ is given only as the indicator of transient stability. The proposed method does not require information on power angle and it does not need to measure the gird voltage.

A. Test 1: Verification of the Improved PTM by VTI Control

In the first test, the improvement in PTM of the proposed asymmetrical VTI control method is verified. In Fig. 12, the experimental results are presented. In this test, at t_0, the GFM inverter is started with a load step from 0 to 1.0 p.u. At t_1, the power reference $P_{\rm ref}$ is intentionally increased from 1.0 to 1.2 p.u.; thus, the SCR of the system falls from 1.05 down to 0.875. From this point, the GFM inverter starts to lose synchronism with the grid, which can be easily found from the dynamic power angle δ. At t_2, the proposed asymmetrical VTI control is enabled manually. In this case, the PTM is increased and a pair of artificial EPs is created for the system. It can be found that the GFM inverter is stabilized with a higher output power (1.2 p.u.) and the synchronism with the grid is restored.

In Fig. 13, the experimental results of the improved PTM in line fault scenario are presented. At t_1, the line fault is emulated and the grid impedance increased from 0.95 to 1.15 p.u.; thus, the SCR of the system falls from 1.05 down to 0.865. For this

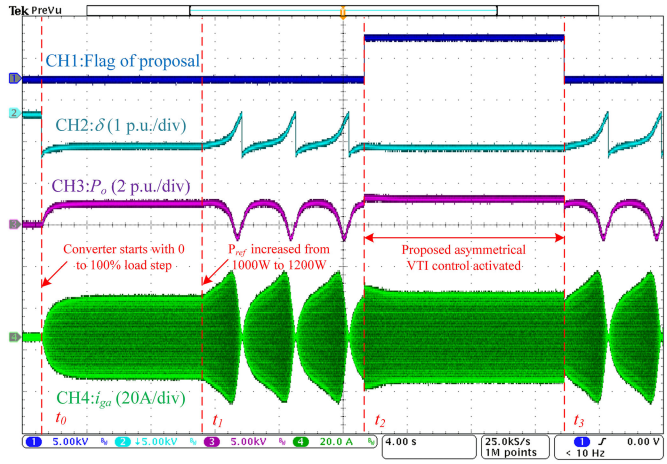

Fig. 12. Experimental results for Test 1 based on increased $P_{\rm ref}$ (1.0–1.2 p.u.).

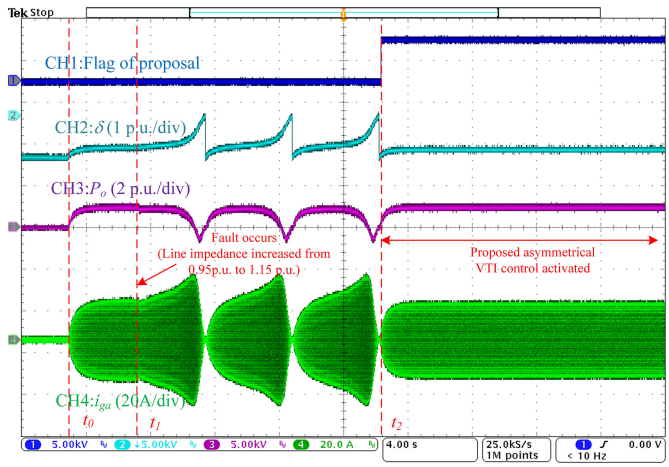

Fig. 13. Experimental results for Test 1 based on increased L_g (0.95–1.15 p.u.).

reason, the GFM inverter starts to suffer from LOS. At t_2, the proposed asymmetrical VTI control is enabled manually. It can be found from the experimental results that the synchronization is restored and the output power is increased to 1.2 p.u. soon after enabling the proposed asymmetrical VTI control method.

By the experimental results shown in Figs. 12 and 13, it can be found that the proposed asymmetrical VTI control can significantly increase the PTM of the GFM inverter under both normal operation and in-fault operation. With such an improvement, the system reobtained a pair of EPs, which make GFM inverter possible to be stabilized and synchronized with the main grid once again during a sever fault. Thus, the transient stability of the GFM inverter can be significantly enhanced.

B. Test 2: Fault-Reaction of the Proposed Control Method

For the fault response in a grid-connected system, the effectiveness and timeliness are equally important. Thus, in the second test, the fault reaction of the proposed control method is the main concern. The effectiveness of the proposed transient instability detector is demonstrated and evaluated in this test.

In Fig. 14, the experimental results of test 2 are presented. In this test, the grid fault is the same as shown in Fig. 14.

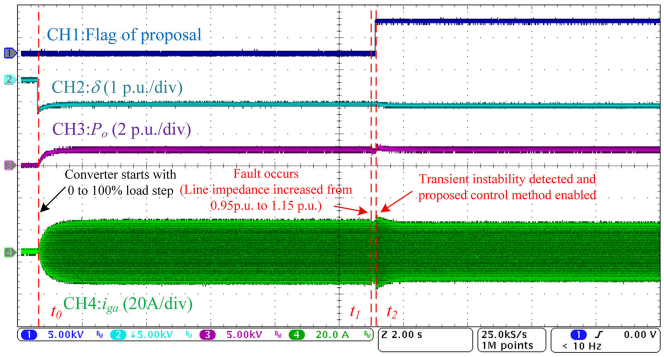

Fig. 14. Experimental results for Test 2 based on emulated transmission line fault (L_g increased from 0.95 to 1.15 p.u.) and nominal time threshold (0.2 s) of the proposed transient instability detector.

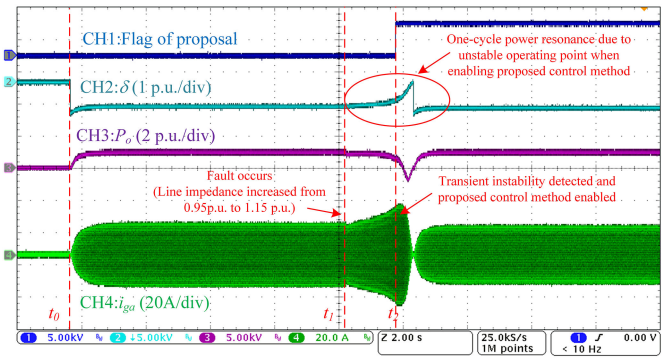

Fig. 15. Experimental results for Test 2 based on emulated transmission line fault (L_g increased from 0.95 to 1.15 p.u.) and intentionally increased time threshold (1.5 s) of the proposed transient instability detector.

However, instead of manually enabling the proposed control method, the proposed transient instability detector is controlling the trigger of the proposed asymmetrical VTI control. In the first test scenario, the time threshold of fault detection is set to be 0.2 s. It can be seen from the experimental results that the proposed detector has a fast response and the LOS issue is eliminated at its early stage. In addition to that, the proposed detector does not trigger at t_0 when the GFM inverter starts with a 100% load step. It indicates that the proposed detection method can distinguish the transient instability phenomenon out of large load swing, which is necessary for practical implementation.

In Fig. 15, the experimental results of another tested scenario are presented. In this case, the time threshold is intentionally increased to a larger value (from 0.2 to 1.5 s) to demonstrate the system response if the transient detection is not sufficiently fast. It can be seen from the experimental results that even if the transient instability detector does not detect the LOS issue at its early stage, the transient instability issue can still be detected within the first resonance cycle. In this case, since the power angle is already in unstable region, the GFM inverter will have one-cycle power resonance and the synchronism with the grid will be restored soon after enabling the proposed method.

It can be seen from the experimental results shown, by adopting the proposed asymmetrical VTI control method, the transient stability issue of the GFM inverter under Type-II serve grid fault that leads to nonexistence of EP can be significantly improved. The GFM inverter can be fully synchronized with the grid, and its power output can be maintained and regulated correctly as normal states.

VI. Conclusion

In this article, a *dq*-frame asymmetrical VTI control approach is proposed to enhance the transient stability of the GFM inverter under Type-II serve grid disturbance. The proposed method features for the unique increase of the during-fault PTM by utilizing two-degree-of-freedom asymmetricity of the *d*- and *q*-axis virtual impedance. By utilizing the joint effort of the transient instability detector and the dedicated asymmetrical VTI proposed in this article, the LOS and periodic power resonance of GFM inverter during transient instability can be prevented at their early stages. The physical mechanism and the design philosophy of the proposed method are presented. The effectiveness of the proposed method is verified by both time-domain simulations and experiments. The results show that the proposed *dq*-frame asymmetrical VTI can increase the during-fault PTM and the proposed method can effectively and timely prevent the GFM inverter from transient instability with a well-regulated constant power output. By adopting the proposed control method, the GFM inverter can work as normal during severe grid fault and provides power and grid support to the local power system, which can be helpful to prevent the system from collapsing or black-out.

References

[1] R. Quint *et al.*, "Transformation of the grid: The impact of distributed energy resources on bulk power systems," *IEEE Power Energy Mag.*, vol. 17, no. 6, pp. 35–45, Nov./Dec. 2019.

[2] Australian Energy Market Operator, "System strength requirements methodology: Inertia requirements & shortfalls," Jul. 1, 2018. [Online]. Available: https://www.aemo.com.au

[3] ENTSO-E, "High penetration of power electronic interfaced power sources and the potential contribution of grid forming inverters," Jan. 30, 2020. [Online]. Available: www.entsoe.eu

[4] ENTSO-E, "Future system inertia—Report prepared by Energienet.dk, Fingrid, Stanett and Svenska Krafnät, Brussels," 2015. [Online]. Available: www.entsoe.eu

[5] R. H. Lasseter, Z. Chen, and D. Pattabiraman, "Grid-forming inverters: A critical asset for the power grid," *IEEE J. Emerg. Sel. Topics Power Electron.*, vol. 8, no. 2, pp. 925–935, Jun. 2020, doi: 10.1109/JESTPE.2019.2959271.

[6] D. Pattabiraman, R. H. Lasseter, and T. M. Jahns, "Comparison of grid following and grid forming control for a high inverter penetration power system," in *Proc. IEEE Power Energy Soc. Gen. Meeting*, 2018, pp. 1–5, doi: 10.1109/PESGM.2018.8586162.

[7] R. Rosso, X. Wang, M. Liserre, X. Lu, and S. Engelken, "Grid-forming inverters: Control approaches, grid-synchronization, and future trends—A review," *IEEE Open J. Ind. Appl.*, vol. 2, pp. 93–109, 2021, doi: 10.1109/OJIA.2021.3074028.

[8] H. Wu and X. Wang, "Design-oriented transient stability analysis of grid-connected inverters with power synchronization control," *IEEE Trans. Ind. Electron.*, vol. 66, no. 8, pp. 6473–6482, Aug. 2019.

[9] X. Wang, M. G. Taul, H. Wu, Y. Liao, F. Blaabjerg, and L. Harnefors, "Grid-synchronization stability of inverter-based resources—An overview," *IEEE Open J. Ind. Appl.*, vol. 1, pp. 115–134, 2020.

[10] H. Xin, L. Huang, L. Zhang, Z. Wang, and J. Hu, "Synchronous instability mechanism of P-f droop-controlled voltage source inverter caused by current saturation," *IEEE Trans. Power Syst.*, vol. 31, no. 6, pp. 5206–5207, Nov. 2016, doi: 10.1109/TPWRS.2016.2521325.

[11] D. Pan, X. Wang, F. Liu, and R. Shi, "Transient stability of voltage-source inverters with grid-forming control: A design-oriented study," *IEEE J. Emerg. Sel. Topics Power Electron.*, vol. 8, no. 2, pp. 1019–1033, Jun. 2020.

[12] P. Kundur *et al.*, "Definition and classification of power system stability IEEE/CIGRE joint task force on stability terms and definitions," *IEEE Trans. Power Syst.*, vol. 19, no. 3, pp. 1387–1401, Aug. 2004, doi: 10.1109/TPWRS.2004.825981.
[13] P. Kundur, *Power System Stability and Control*. New York, NY, USA: McGraw-Hill, 1994, pp. 827–836.
[14] X. Hou, H. Han, C. Zhong, W. Yuan, M. Yi, and Y. Chen, "Improvement of transient stability in inverter-based AC microgrid via adaptive virtual inertia," in *Proc. IEEE Energy Convers. Congr. Expo.*, 2016, pp. 1–6.
[15] Z. Liu and Z. Zhang, "Reinforcement learning-based parameter tuning for virtual synchronous machine on grid transient stability enhancement," in *Proc. 46th Annu. Conf. IEEE Ind. Electron. Soc.*, 2020, pp. 4069–4075.
[16] Y. Ma, L. Zhu, F. Wang, and L. M. Tolbert, "Enhancing power system transient stability by virtual synchronous generator control using wide-area measurements," in *Proc. IEEE Energy Convers. Congr. Expo.*, 2019, pp. 2546–2551.
[17] H. Wu and X. Wang, "A mode-adaptive power-angle control method for transient stability enhancement of virtual synchronous generators," *IEEE J. Emerg. Sel. Topics Power Electron.*, vol. 8, no. 2, pp. 1034–1049, Jun. 2020.
[18] T. Qoria, F. Gruson, F. Colas, G. Denis, T. Prevost, and X. Guillaud, "Critical clearing time determination and enhancement of grid-forming inverters embedding virtual impedance as current limitation algorithm," *IEEE J. Emerg. Sel. Topics Power Electron.*, vol. 8, no. 2, pp. 1050–1061, Jun. 2020.
[19] F. Welck, D. Duckwitz, and C. Gloeckler, "Influence of virtual impedance on short circuit performance of virtual synchronous machines in the 9-bus system," in *Proc. NEIS Conf. Sustain. Energy Supply Energy Storage Syst.*, 2017, pp. 1–7.
[20] X. Hou, H. Han, C. Zhong, W. Yuan, M. Yi, and Y. Chen, "Improvement of transient stability in inverter-based AC microgrid via adaptive virtual inertia," in *Proc. IEEE Energy Convers. Congr. Expo.*, 2016, pp. 1–6.
[21] Z. Liu and Z. Zhang, "Reinforcement learning-based parameter tuning for virtual synchronous machine on grid transient stability enhancement," in *Proc. IECON 2020 46th Annu. Conf. IEEE Ind. Electron. Soc.*, 2020, pp. 4069–4075.
[22] Z. Jin, X. Wang, F. Liu, K. Xin, and Y. Liu, "A voltage-droop-free reactive power sharing solution in microgrids," in *Proc. IEEE 9th Int. Power Electron. Motion Control Conf.*, 2020, pp. 3323–3328, doi: 10.1109/IPEMC-ECCEAsia48364.2020.9367665.
[23] O. V. Kulkarni, S. Doolla, and B. G. Fernandes, "Simple controller configuration for decentralized parallel operation of inverters," *IEEE Trans. Power Electron.*, vol. 34, no. 2, pp. 1356–1369, Feb. 2019.
[24] Z. Jin, X. Wang, Y. Liao, D. Yang, A. Burstein, and E. de Jong, "Near-synchornous resonance interaction of paralleled grid-forming converters in islanded operation," in *Proc. 4th IEEE Workshop Electron. Grid*, 2019, pp. 1–6.
[25] Y. W. Li and C. Kao, "An accurate power control strategy for power-electronics-interfaced distributed generation units operating in a low-voltage multibus microgrid," *IEEE Trans. Power Electron.*, vol. 24, no. 12, pp. 2977–2988, Dec. 2009.
[26] K. Bimal, *Modern Power Electronics and AC Drives*. Englewood Cliffs, NJ, USA: Prentice-Hall, 2001.

Zheming Jin (Member, IEEE) was born in Jilin, China. He received the B.S. degree in electrical engineering and the M.S. degree in power electronics and ac drives from Beijing Jiaotong University, Beijing, China, in 2013 and 2015, respectively, and the Ph.D. degree in power electronic systems from the Department of Energy Technology, Aalborg University, Aalborg, Denmark, in 2018.

In 2019, he joined the Department of Energy Technology, Aalborg University, as a Postdoctoral Researcher, and was subsequently appointed as an Assistant Professor. In 2021, he joined Beijing Jiaotong University, where he is currently an Associate Professor. His research interests include control of power electronic converters, stability of power electronic systems, energy storage, dc microgrids, and their applications in transportation electrification.

Xiongfei Wang (Senior Member, IEEE) received the B.S. degree in electrical engineering from Yanshan University, Qinhuangdao, China, in 2006, the M.S. degree in electrical engineering from the Harbin Institute of Technology, Harbin, China, in 2008, and the Ph.D. degree in energy technology from Aalborg University, Aalborg, Denmark, in 2013.

From 2009, he has been with the Department of Energy Technology, Aalborg University, where he became an Assistant Professor in 2014, an Associate Professor in 2016, and a Professor and Leader of Electronic Power Grid (eGRID) Research Group in 2018. He has also been a part-time Professor with the KTH Royal Institute of Technology, Stockholm, Sweden, since 2020. His research interests include modeling and control of power electronic converters and systems, stability and power quality of power-electronics-dominated power systems, and high-power converters.

Dr. Wang is a Member-at-Large of Administrative Committee for the IEEE Power Electronics Society (PELS) from 2020 to 2022, a Co-Editor-in-Chief for the IEEE TRANSACTIONS ON POWER ELECTRONICS LETTERS, and as an Associate Editor for the IEEE JOURNAL OF EMERGING AND SELECTED TOPICS IN POWER ELECTRONICS. He was selected into Aalborg University Strategic Talent Management Program in 2016. He was the recipient of six Prize Paper Awards in the IEEE transactions and conferences, the 2018 Richard M. Bass Outstanding Young Power Electronics Engineer Award, the 2019 IEEE PELS Sustainable Energy Systems Technical Achievement Award, the 2020 IEEE Power & Energy Society Prize Paper Award, the 2020 IEEE JOURNAL OF EMERGING AND SELECTED TOPICS IN POWER ELECTRONICS Star Associate Editor Award, and the Highly Cited Researcher in the Web of Science in 2019–2021.